

Electrochemical Infrared Characterization of Carbon-Supported Platinum Nanoparticles: A Benchmark Structural Comparison with Single-Crystal Electrodes and High-Nuclearity Carbonyl Clusters

Sungho Park, Sally A. Wasileski, and Michael J. Weaver*

Department of Chemistry, Purdue University, West Lafayette, Indiana 47907-1393

Received: May 17, 2001

Electrode potential-dependent infrared spectra for carbon monoxide dosed onto carbon-supported platinum nanoparticle films, significant as commercial fuel-cell catalysts as well as of fundamental importance, are reported with the aim of elucidating their structure as a function of particle size. The need to acquire absolute unipolar, rather than bipolar, spectra by means of potential-difference infrared tactics for such nanoparticle films is demonstrated, given the broad asymmetric C–O stretching band shapes. For larger particle diameters ($d \geq 4$ nm), the potential-dependent peak stretching frequencies (ν_{CO}^P) for saturated CO are closely similar to atop CO on Pt(111) electrodes, indicating a preponderance of 9-coordinate Pt sites. However, for nanoparticle diameters in the range $d \approx 2$ –4 nm, the ν_{CO}^P values at a given potential, E , redshift sharply with decreasing d , approaching frequencies compatible with those measured at the same surface potential for atop CO in chargeable high-nuclearity Pt carbonyl solutes. The latter, structurally well-characterized, nanoparticles are known to contain predominantly edge- rather than (111) terrace-bound CO. The implication that the nanoparticle size-dependent structural transition is associated with changes in the Pt surface coordination number, consistent with pseudo-spherical packing-density considerations, is supported by comparisons of the ν_{CO}^P – E data for lower CO coverages with corresponding potential-dependent spectra for CO bound to step sites on high-index Pt electrodes. The broad-based value of vibrational measurements at controlled surface potentials for characterizing conducting nanomaterials is pointed out.

Introduction

Understanding how the chemical coordinative and catalytic properties of metal nanoparticles depend on their size and shape is a major contemporary theme in surface chemistry. As an important technological example, the demonstrated value of carbon-supported Pt-group nanoparticles as electrodes in methanol–air fuel cells earmarks them as key materials worthy of detailed fundamental examination.¹ Significantly, the electrocatalytic properties of the C/Pt electrodes are sensitive to the nanoparticle size over the diameter range, ca. 2–10 nm, relevant to the commercial fuel-cell materials.^{1,2} Nanoparticle size effects have been reported recently by the Illinois group on the basis of ¹³C NMR measurements upon chemisorbing ¹³CO (from methanol dissociation) on these materials, and interpreted in terms of variations in the metal Fermi-level density-of-states.³ Correlations were also attempted between the particle size-dependent NMR results and infrared spectra, specifically the C–O stretching (ν_{CO}) frequencies.⁴ However, interpretation of the latter is limited by the bipolar form of the ν_{CO} spectra extracted with the potential-difference technique used in ref 4 (vide infra), together with uncertainties in the CO coverages produced by methanol dissociation.

We have been interested for some time in probing the chemisorption of carbon monoxide and related species on oriented monocrystalline Pt-group electrodes by using electrochemical infrared reflection–absorption spectroscopy (EC-IRAS) (for example, refs 5–10). The EC-IRAS technique employed in all these studies entails recording a single “refer-

ence spectrum” at an electrode potential where CO is electrooxidatively removed, thereby yielding absolute (unipolar) ν_{CO} bands, as obtained commonly at metal–ultrahigh vacuum (UHV) interfaces.^{5,11,12} A major motivation is to relate the structure and bonding properties of electrochemical interfaces to the better-understood metal surfaces in UHV.^{8–10} This work has led to a quantitative understanding of the often-substantial differences in ν_{CO} frequencies as well as CO binding configurations observed at Pt-group electrodes versus their UHV-based counterparts. A critical factor is the lower surface potentials (typically $\Delta\phi_s \sim 1$ –2 V) generated at the former interfaces by double-layer solvation, yielding markedly (up to 100 cm^{−1}) redshifted ν_{CO} frequencies via the vibrational Stark effect.^{9,10} Related properties are also evident in the charge-dependent ν_{CO} spectra of high-nuclearity platinum carbonyls, (Pt_{*x*}CO_{*y*})^{*n*} ($x = 24, 26, 38, n = 0$ to -10), examined earlier in our laboratory by infrared spectroelectrochemistry.^{13,14} These systems provide uniquely well-characterized examples of chargeable small (~ 1 nm diameter) nanoparticles in solution.^{13,14}

Armed with such rich information relating electrochemical ν_{CO} spectra with surface structure, we have ventured to examine corresponding electrode potential-dependent spectra for CO chemisorbed on carbon-supported Pt nanoparticles with the aim of forging a structural interpretation of their size-dependent properties. By depositing ultrathin (ca. 1–2 monolayer) films of the commercial C/Pt films on polished gold, we are able to obtain “absolute” ν_{CO} absorbance spectra that are largely free of the anomalous bipolar and inverted infrared band effects that are commonly observed for thicker densely packed films,¹⁵ which complicate the chemical interpretation. The salient

* Corresponding author. E-mail: mweaver@purdue.edu.

infrared spectral findings and structural interpretation are presented herein. They indicate a central role of the metal surface coordination number in controlling the Pt nanoparticle properties. We present elsewhere, in collaboration with the Illinois group, a comparison between the potential-dependent IRAS properties of CO formed by direct CO dosing and methanol dissociation on these materials, with an eye toward linking more closely their infrared and NMR properties.^{16a}

Experimental Section

Most experimental details of the EC-IRAS measurements are available elsewhere.^{6,12} The FTIR spectrometer was a Mattson RS-2 instrument, with a custom-built external reflection compartment containing the narrow-band MCT detector. The metal gold disk substrate, (ca. 0.9 cm diameter) mounted on a glass plunger by wrapping with Teflon tape, was pressed against the CaF₂ window forming the base of the spectroelectrochemical cell so as to create the optical thin layer.

The C/Pt films were prepared by depositing a dilute suspension (3 mg/mL) of the material (purchased from E-Tek, Inc, Natick, MA) via a microsyringe onto the polished gold substrate diluting with additional water droplets so to spread the C/Pt evenly over the surface, followed by drying by argon flow for ca. 3 min and rinsing with a jet of ultrapure water to remove loosely held particles. The resulting surface contains a thin, relatively uniform, and very reproducible C/Pt film which provides excellent voltammetric as well as IRAS characteristics, the latter being aided by its highly reflective nature. A key feature of the C/Pt film preparation for EC-IRAS purposes is the rinsing stage (vide infra).^{16b} Carbon monoxide (99.99% min, Matheson Gases), was dispensed from an aluminum cylinder (to avoid iron carbonyl impurities), and supporting electrolytes were prepared from double-distilled H₂SO₄ or HClO₄ (G. F. Smith) using ultrapure water from a Millipore MillQ system. Electrode potentials were measured and are reported here vs a Ag/AgCl(sat. KCl) reference electrode (Bioanalytical Systems).

The Density Functional Theory (DFT) calculations described in footnote 31 were undertaken largely as described in ref 17. Briefly, they utilized the Amsterdam Density Functional (ADF) package,^{18a,b} with the BP86 functional. The required ν_{CO} stretching frequencies for selected atop CO binding geometries were calculated using the AnharMND program^{18c} from a potential-energy surface involving ca. ± 0.2 Å displacements from the determined equilibrium bond lengths.

Results and Discussion

Cyclic Voltammetry. A typical voltammogram for a C/Pt (60% loading) film (average particle diameter, $d \approx 8.8$ nm) is shown as the solid trace in Figure 1A, acquired (at 50 mV s⁻¹) from -0.25 to 0.8 V vs Ag/AgCl in 0.05 M H₂SO₄, encompassing the characteristic hydrogen adsorption and oxide formation regions below 0 V and above ca. 0.5 V, respectively. A rough estimate of the effective Pt nanoparticle surface area is obtained from the reversible hydrogen charge, comparable to (within ca. 2-fold of) that for a conventional polycrystalline Pt electrode. A corresponding voltammogram for the latter is shown for comparison in Figure 1B. The most reproducible voltammetric (and IRAS) response for the nanoparticle films was obtained following a few potential cycles between -0.25 and 0.4 V. Thicker C/Pt films, yielding 5–10-fold higher hydrogen adsorption charges, could also be formed on gold, most readily by omitting the rinsing step mentioned above. However, while the voltammetric characteristics are similar, as noted below the IRAS response then exhibits anomalous effects.^{16b}

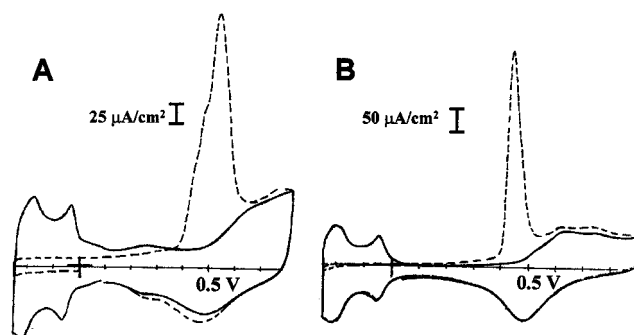


Figure 1. Comparison between cyclic voltammograms (50 mV s⁻¹) on: (A) C/Pt (60% loading) film on gold, and (B) conventional polycrystalline Pt electrode, in 0.05 M H₂SO₄ alone (solid traces) and with saturated CO layer (dashed traces). Electrode potentials are versus Ag/AgCl.

The corresponding dashed traces in Figure 1 show the anodic–cathodic voltammetric responses following a saturated dosage of chemisorbed CO, obtained by bubbling in gaseous CO followed by argon sparging. The charge contained under the anodic peak for adsorbed CO electrooxidation, q_{CO} , in relation to the adsorbed hydrogen charge, q_H , provides a rough measure of the CO coverage normalized to the Pt atomic density, $\theta_{CO} \approx 0.5q_{CO}/q_H$ (vide infra). Besides the 60% Pt film ($d \approx 8.8$ nm), we also examined the voltammetric behavior of C/Pt films with 40, 30, 20, and 10% loading, corresponding to average particle diameters of 3.9, 3.2, 2.5, and 2.0 nm, respectively, as determined from transmission electron microscopy (TEM).^{3,4} Comparable voltammetric responses were obtained in each case, although the hydrogen peak at ca. -0.05 V became less discernible with decreasing Pt particle size.^{16a,b} Similar size-dependent voltammetric profiles have also been observed for electrodeposited Pt nanoparticles.¹⁹

Infrared Spectral Acquisition Tactics. Prior to considering the nanoparticle size-dependent EC-IRAS data, it is necessary to clarify the importance of extracting absolute ν_{CO} spectra for these systems using conventional potential-difference infrared (PDIR) tactics.^{11,12} Two variants of PDIR are in common use for conventional electrode materials, both aimed at removing solution-phase spectral interferences.^{11,12} The first, more desirable, approach (termed here Method I) entails recording a “reference” spectrum at an electrode potential where the adsorbate of interest is entirely removed, either by oxidation/reduction or desorption. Even if this process is irreversible (such as for CO electrooxidation), subtracting the reference spectrum from those acquired immediately beforehand at the electrode potential(s) of interest can yield the desired adsorbate absolute spectra for the latter condition.^{20a}

Pairs of ν_{CO} absorbance spectra obtained by using Method I for saturated irreversibly adsorbed CO adlayers at 0 V (a) and -0.2 V (b) on a C/Pt film (60% loading) and on a polycrystalline Pt electrode [Pt(poly)] are compared in Figs. 2A and B, respectively. The reference spectrum in both cases was obtained subsequently at 0.65 V after CO electrooxidation was complete; each spectrum was acquired from 100 interferometer scans. Immediately noticeable is the presence of a broad “tail” on the Pt nanoparticle ν_{CO} spectra toward lower wavenumbers (Figure 2A), which is essentially absent from the corresponding atop CO band on Pt(poly) (Figure 2B). As discussed below, this feature can be attributed to CO binding on smaller nanoparticle fragments. Also evident in Figure 2A is a small “negative-going” absorbance component at slightly higher frequencies than the ν_{CO} absorbance peak. This feature grows markedly with increasing C/Pt film thickness,^{16b} and is symptomatic of the

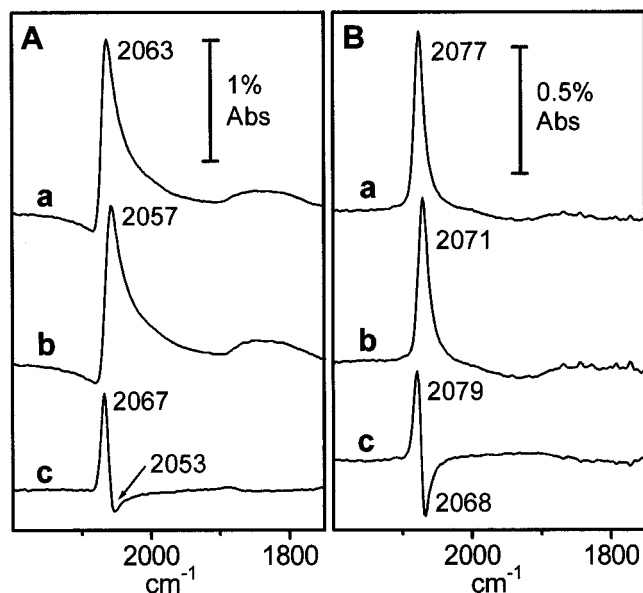


Figure 2. Comparison between “absolute” and “bipolar” potential-difference infrared (PDIR) absorbance spectra obtained by Methods I and II, respectively (see text), for saturated CO layers on (A) C/Pt (60% loading) film and (B) conventional polycrystalline Pt electrode. Spectra (a) and (b) in each case are “absolute” ν_{CO} spectra (Method I) obtained at 0 V and -0.2 V vs Ag/AgCl, respectively, using a “reference spectrum” obtained upon complete CO electrooxidation at 0.65 V. Spectra (c) are obtained from the spectral difference between 0 and -0.2 V, i.e., spectra (a) minus (b).

occurrence of “inverted infrared absorbance”, apparently associated with the anomalous dielectric properties of aggregated metal particles.^{15a} This effect, which can result in partial band interferences and other spectral complications,¹⁵ is mimized by the present use of ultrathin (1–2 equivalent monolayer) films.

In the alternative PDIR approach (dubbed here Method II), spectra are obtained at pairs of electrode potentials within the region where the adsorbate is stable, spectral subtraction again being employed.^{12,20b} This tactic, employed for example in ref 4, enables repeated potential modulation to be undertaken, in some cases enhancing the spectral sensitivity. However, the potential-induced band wavenumber shift (vibrational Stark effect) needs to be sufficient to avoid substantial mutual interference between the two components of the resulting bipolar infrared bands. Importantly, this requirement is *not met* for the Pt nanoparticle films. Spectra (c) in Figure 2, parts A and B, are PDIR data obtained using Method II on the C/Pt film and Pt(poly) as before, employing the same pair of potentials, 0 V and -0.2 V, to which (a) and (b) refer. Consequently, spectra (c) equals (a) minus (b).

Comparison between the corresponding bipolar spectra (c) and the “absolute” spectra (a) and (b) in Figure 2, parts A and B, demonstrates the key point. For the Pt(poly) electrode (Figure 2B), as for other planar macroscopic surfaces, the ν_{CO} bands are sufficiently narrow so to yield bipolar spectra, such as (c), that retain some identifiable contributions from the absolute band components (a) and (b) at the two electrode potentials. For the C/Pt film electrode (Figure 2A), on the other hand, the broader and markedly asymmetric nature of the component bands (a) and (b) yield bipolar spectra (c) with sufficiently serious band interference toward lower wavenumbers so that much of the spectral information is obscured. Consequently, the use of this approach for examining nanoparticle infrared spectra, as undertaken recently for C/Pt films,⁴ can be fraught with difficulty.^{16a} Only absolute ν_{CO} spectra extracted via Method I are therefore considered here.

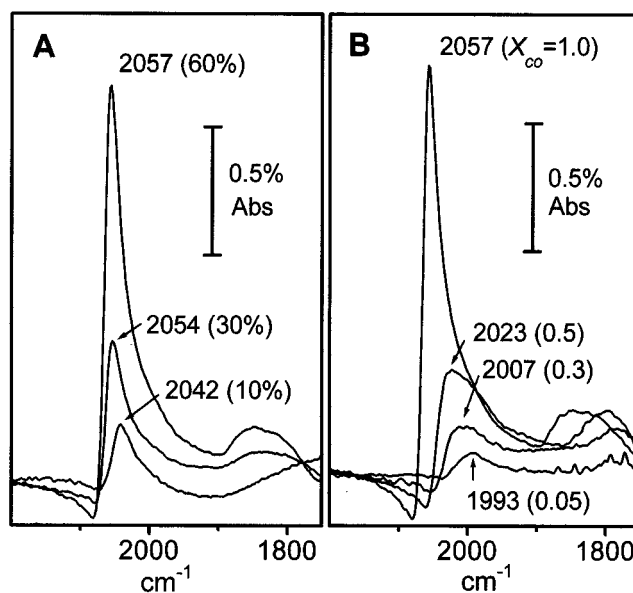


Figure 3. Selected infrared absorbance spectra at -0.2 V vs Ag/AgCl for: (A) saturated CO packing densities ($X_{\text{CO}} = 1$) on C/Pt films (60, 30, 10% loading, as indicated), (B) different subsaturated packing densities (X_{CO} , as indicated in parentheses) for C/Pt (60% loading) film.

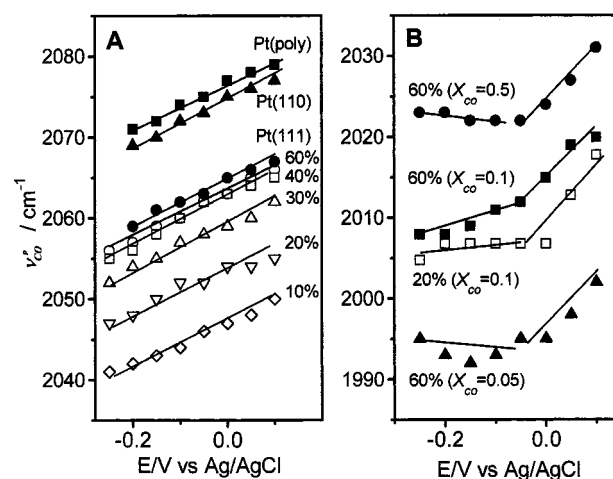


Figure 4. Peak ν_{CO} frequencies versus electrode potential for: (A) saturated CO adlayer on macroscopic Pt electrodes compared with C/Pt films, as indicated; (B) sub-saturated CO packing densities (X_{CO} , as indicated in parentheses) on C/Pt films.

Nanoparticle Size-Dependent Spectra. Of central interest is the detailed nature of the ν_{CO} absorbance spectra for the C/Pt film electrodes as a function of the nanoparticle size. Figure 3A shows typical spectra obtained for saturated CO dosages for three nanoparticle loadings (60, 30, and 10%, as indicated), at -0.2 V vs Ag/AgCl. (We denote such saturated layers hereafter as having a “fractional packing density”, X_{CO} , of unity.) As exemplified in Figure 2A, closely similar ν_{CO} band shapes were obtained over the potential (E) range -0.25 to 0.2 V prior to the onset of CO electrooxidation, except for the usual ν_{CO} frequency– E (Stark-tuning) shift. The peak ν_{CO} frequency ($\nu_{\text{CO}}^{\text{P}}$) versus E plots obtained for each nanoparticle film, along with corresponding data for saturated CO adlayers on Pt(111), Pt(110), and Pt(poly) electrodes, are shown in Figure 4A. (The monocrystalline electrode data were obtained earlier in this laboratory.^{5,9a,b}) While the data presented here refer to 0.05 M H_2SO_4 electrolyte, essentially identical spectra were obtained also in 0.1 M HClO_4 .

Close inspection of the spectral data in Figures 3A and 4A reveals several important features. Most significantly, ν_{CO}^P redshifts as the particle size decreases, especially below ca. 4 nm (40% loading). (The spectrum for the 40% loading film is omitted from Figure 3A since it is closely similar to that for the 60% film.) However, the ν_{CO}^P - E slopes, 25–30 $\text{cm}^{-1} \text{V}^{-1}$, are insensitive to the particle size, also being similar to those observed for saturated CO adlayers on the macroscopic Pt electrodes (Figure 4A). Similarly to the 60% film, the ν_{CO} spectra for the smaller nanoparticles exhibit a lower-wavenumber “tail”, although the overall bandwidth narrows with decreasing particle size (Figure 3A). The ν_{CO} wavenumber range, ca. 2000–2060 cm^{-1} , is indicative of atop CO, i.e., bound to a single Pt atom. The larger Pt nanoparticles also exhibit a broad weaker ν_{CO} band around 1820–1840 cm^{-1} (Figure 3A), consistent with the secondary presence of twofold-bridging CO.⁷ A similar feature is also evident on Pt(111) electrodes^{6,11} and for high-nuclearity Pt carbonyl clusters.^{13,14}

Spectral data were obtained for a range of sub-saturated CO packing densities (i.e., $X_{CO} < 1$) formed by dosing the nanoparticle films with diluted (ca. 10^{-5} M) CO solutions for controlled times, typically ≤ 2 min. (The same tactic is used to generate lower dosed CO coverages on planar Pt electrodes.⁵) The fractional packing densities, X_{CO} , were obtained from the absorbance of the CO_2 band at 2345 cm^{-1} observed in the PDIR spectra upon complete CO electrooxidation in the absence of significant solution CO_2 ²¹ relative to its value for a saturated layer ($X_{CO} = 1$). [The CO_2 remains trapped in the thin layer on the time scale (ca. 1–2 min) of the spectral measurements.^{21,22}] Representative X_{CO} -dependent spectra obtained at -0.2 V for a 60% loading film are shown in Figure 3B. The ν_{CO} frequencies at low X_{CO} are seen to be strongly redshifted (by 60–70 cm^{-1}) below the monolayer values, lying within the low-frequency “tail” of the latter spectra. The structural significance of these data is considered below.

Another interesting aspect concerns the integrated ν_{CO} band absorbances, A_{CO} . Comparison between the absolute ν_{CO} spectra for saturated CO on the 60% loading film and Pt(poly) in Figure 2, parts A and B [either spectra (a) or (b)], reveals that the A_{CO} value for the former is markedly (ca. 5-fold) larger than the latter even though the Pt surface area (as deduced from the voltammetric hydrogen charge q_H) is comparable. This suggests that the infrared absorption for the nanoparticle film is enhanced relative to that for a planar metal surface. Such “infrared surface enhancement” has been noted previously for various types of deposited films and roughened metal surfaces consisting of particle arrays, including Pt particles.^{15,23,24}

It is useful to define an “infrared enhancement factor”, EF , for CO chemisorbed on the Pt nanoparticle films relative to a planar Pt surface as

$$EF = [A_{CO}(\text{film})/N_{CO}(\text{film})]/[A_{CO}(\text{plane})/N_{CO}(\text{plane})] \quad (1)$$

where $N_{CO}(\text{film})$ and $N_{CO}(\text{plane})$ refer to the number of CO molecules contained in a given cross-sectional area of the film and planar Pt electrodes, respectively, and $A_{CO}(\text{film})$ and $A_{CO}(\text{plane})$ are the corresponding ν_{CO} band absorbances. A reliable measure of $[N_{CO}(\text{film})/N_{CO}(\text{plane})]$ can be obtained readily from the relative CO_2 band absorbances in the PDIR spectra resulting from CO electrooxidation.^{21,22}

Values of EF for the present Pt nanoparticle films extracted from eq 1 in this fashion, using the Pt(poly) electrode as a “reference planar” surface, are listed in Table 1. [Closely similar EF values are obtained when employing instead monocrystalline Pt electrodes, such as Pt(111), as the reference planar surface.]

TABLE 1: Nanoparticle-CO Packing Densities, Coverages, and Infrared Enhancement Factors

Pt loading	X_{CO}^a	$\theta_{CO}(\text{sat})^b$	EF^c
60%	1.0	~ 1.2	7
	0.5		5
	0.3		4.5
40%	1.0	~ 1.2	6
30%	1.0	1.4	4
20%	1.0	1.5	3
	0.2		4
10%	1.0	~ 1.7	2

^a Fractional adsorbate packing density, defined as $X_{CO} = 1$ at saturation. Sub-saturated values determined from ratio of CO_2 infrared absorbance band obtained upon adsorbed CO electrooxidation normalized to that where $X_{CO} = 1$. ^b Saturated CO coverage, defined as ratio of CO surface density to that of available Pt sites, the latter being determined from the voltammetric hydrogen charge and from spectro-electrochemical CO/CO_2 band intensities (see text for further details).

^c Infrared enhancement factor, determined from infrared absorbance data by using eq 1 (see text).

The majority of EF values given refer to saturated CO layers, denoted as a “fractional packing density” $X_{CO} = 1.0$. Examples are also included for lower X_{CO} values (again extracted from the CO_2 absorbance relative to the saturated value), formed by controlled-time dosing from diluted CO solutions (vide infra). While the EF values do not vary greatly with X_{CO} , they decrease monotonically toward lower Pt loadings (Table 1), the greatest enhancements (ca. 5–10) therefore being obtained for the largest nanoparticles. This trend is consistent with the predictions of a dielectric model where greater infrared absorbance enhancements arise for increasing metal particle film densities due to their optical interaction.^{15a} (This is the same model that accounts for the observed anomalous bipolar and inverted absorbance behavior for particle aggregates,^{15a} vide supra.)

Structural Interpretation of Nanoparticle Spectra. Examination of the ν_{CO} frequencies and bandwidths for the Pt nanoparticles in comparison with both monocrystalline Pt electrodes and high-nuclearity Pt carbonyl clusters provides key structural insight. A central notion, stressed repeatedly in IRAS analyses of CO (and NO) adlayers on single-crystal surfaces in electrochemical versus UHV-based systems, is the desire to undertake such comparisons using vibrational frequencies measured at an equivalent surface potential, ϕ_s .^{8,9} (The ϕ_s equivalence in such cases can be achieved by adjusting the applied electrode potential in the former systems so to match the measured work function for the latter, with a knowledge of the “absolute” reference electrode potential.^{8,9}) Matching up the system surface potentials in this fashion essentially removes the often-dominant ν_{CO} frequency variations due to electrostatic field (Stark) effects, revealing the distinct influence of more “chemical bonding” environmental effects on the surface vibrational spectra, such as changes in surface coordination geometry.⁹ [As mentioned above, the typically 1–2 V lower values of ϕ_s in electrochemical versus UHV environments result in markedly (up to ca. 100 cm^{-1}) lower ν_{CO} frequencies via the vibrational Stark effect.]

In the present case involving only nanoparticle–solution and planar metal–solution interfaces, the ν_{CO} spectral comparisons most simply utilize a common electrode potential taken in the median range of accessible values. Figure 5 contains a plot of the ν_{CO}^P values measured at 0 V vs Ag/AgCl for each nanoparticle film examined here versus the average particle diameter, d (filled circles). Included at the left extremity of this plot is a point (filled triangle) for $(\text{Pt}_{26}\text{CO}_{32})^{n-}$, obtained for this small ($d \sim 1 \text{ nm}$) chargeable nanoparticle at an “equivalent elec-

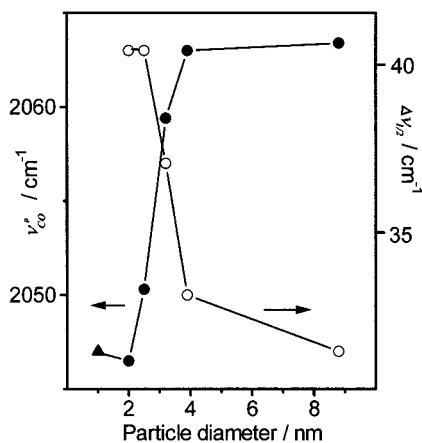


Figure 5. Plot of peak ν_{CO} frequencies (filled circles) and ν_{CO} bandwidth (open circles) for saturated CO adlayers on C/Pt films at 0 V vs Ag/AgCl versus average particle diameter. The filled triangle is ν_{CO}^p value for $(\text{Pt}_{26}\text{CO}_{32})^{n-}$ in dichloromethane at the same potential (see text).

trode potential" in nonaqueous solvents from data in ref 13 (see footnote 25 and below). Similar ν_{CO}^p - d behavior is also obtained by choosing other fixed electrode potentials for the comparison. Intriguingly, the ν_{CO}^p frequencies are seen to undergo a *transition* from values, for $d > 4$ nm, close to those for saturated CO on Pt(111) terraces (Figure 3A), to ca. 20 cm^{-1} lower frequencies, at $d \leq 2$ nm, characteristic of the small Pt carbonyl clusters.

A crucial virtue of the latter systems is that the metal core and CO binding geometries are known quantitatively from X-ray crystallography.^{13,26} Unlike the Pt(111) terrace atoms, which have a surface coordination number, CN , equal to 9, $\text{Pt}_{26}\text{CO}_{32}$ contains chiefly "edge" (or "vertex") sites, where $CN \approx 6-7$, so that most (84%) of the atop CO molecules are bound to the lower-coordination sites rather than within the small (111) facets.^{13,26} A number of studies, primarily for high-index monocrystalline Pt surfaces in UHV, have established that CO bound to step or edge sites exhibit ν_{CO} values that are redshifted significantly (ca. $20-30 \text{ cm}^{-1}$) from terrace-bound atop CO (for example, refs 27-29). Roughly linear ν_{CO}^p - CN correlations have been reported for both low- and high-coverage conditions,²⁹ reflecting increasing $d\pi-2\pi^*$ back-donation associated with stronger metal-CO binding for smaller CN values.³⁰ The ν_{CO} frequencies extracted by using finite-cluster DFT calculations for atop CO in different Pt coordination geometries also yielded essentially concordant behavior.³¹ A detailed DFT study of CO chemisorbed on various step and kink, compared to terrace, Pt sites shows that the stronger CO binding at the former are associated with an increase in the d -band center energy, and hence the local Fermi-level density of states (vide infra).³⁰

Comparable ν_{CO}^p redshifts have been established for edge-versus terrace-bound CO on stepped monocrystalline Pt electrodes in aqueous solution, but again with the important modification that the terrace-, and especially edge-, bound CO exhibit ν_{CO}^p values substantially (ca. $30-60 \text{ cm}^{-1}$) redshifted from UHV-based frequencies due to the Stark effect.³² Although the ν_{CO}^p value for $(\text{Pt}_{26}\text{CO}_{32})^{n-}$ at 0 V, 2047 cm^{-1} , included in Figure 5, is ca. $30-35 \text{ cm}^{-1}$ higher than for low-coverage CO bound to stepped Pt electrodes at the same potential,³² this difference is largely accommodated for by dipole-dipole coupling in the former high-coverage condition.

The sharp ν_{CO}^p decreases seen for $d < 4$ nm in Figure 5 can therefore be attributed with confidence to a transition from

predominantly (111) terrace to edge-site CO binding for the smaller C/Pt nanoparticles. Significantly, it is *precisely* this size range $d \approx 2-4$ nm where a transformation from chiefly terrace Pt surface atoms ($CN = 9$) to smaller particles featuring chiefly edge (and vertex) sites is expected on the basis of ideal icosahedral and related metal packing arrangements where the particles assume pseudo-spherical shapes.^{1,33} The increased Pt-OH and Pt-CO binding energies on the smaller nanoparticles ($d < 4$ nm) as implied from X-ray absorption studies^{1,2} are also consistent with the increasing dominance of edge/vertex Pt sites.

Another sign of increasing edge-site coordination in small nanoclusters is that higher CO packing densities can be achieved, as clearly manifested in the $\text{Pt}_{24}\text{CO}_{30}$ and $\text{Pt}_{26}\text{CO}_{32}$ clusters, which feature CO/surface Pt ratios (θ_{CO}) of 1.3 and 1.5, respectively; by comparison, the saturated θ_{CO} value, $\theta_{CO}(sat)$, on Pt(111) is only 0.75.⁷ Estimates of $\theta_{CO}(sat)$ were also obtained for the present nanoparticle films in two ways. The first method, already mentioned, involves evaluating the voltammetric charge for two-electron CO electrooxidation, q_{CO} , in relation to the adsorbed hydrogen charge, q_H . The resulting $\theta_{CO}(sat)$ values ($= 0.5 q_{CO}/q_H$) are only approximate due primarily to uncertainties in equating q_{CO} with the faradaic charge for CO electrooxidation.²² The second approach entails utilizing the spectrophotometric CO_2 band intensity for a given film relative to that for a planar Pt surface normalized to the relative hydrogen charges.

Average estimates of $\theta_{CO}(sat)$ obtained with these two methods are given in Table 1. [Note the distinction between θ_{CO} and X_{CO} : while $\theta_{CO}(sat)$ varies with the particle/surface geometry, for such saturated adlayers we *define* that $X_{CO} = 1$.] While the values are only approximate using both methods (ca. $\pm 25\%$), $\theta_{CO}(sat)$ clearly increases as the nanoparticle size decreases. However, the $\theta_{CO}(sat)$ values obtained for the smallest film loadings, 1.5-1.7, are higher than those for the structurally defined nanoclusters just mentioned. Most likely this reflects the polydispersed nature of the commercial film materials, with partial fragmentation to yield a fraction of particles that are markedly smaller than the average d values extracted from TEM.^{1,3,4} A qualitatively similar CO coverage effect has been noted for colloidal platinum films on gold electrodes.³⁴

Further insight into the distribution of metal-binding geometries available for the C/Pt nanoparticle films was obtained from the ν_{CO} spectra for a range of sub-saturated CO coverages [$X_{CO} = \theta_{CO}/\theta_{CO}(sat)$], noted above, as exemplified for the 60% loading film in Figure 3B. The extent of the observed redshift, ca. $60-70 \text{ cm}^{-1}$, of ν_{CO}^p seen toward low coverage is markedly beyond that ($20-30 \text{ cm}^{-1}$) expected on the basis of θ_{CO} -induced dipole-dipole coupling,^{5a} signaling preferential low-coverage binding on nanoparticle edge sites. However, icosahedral nanoparticles having the average (8.8 nm) diameter observed by TEM for 60% loading should exhibit chiefly (111) terrace sites.^{1,33}

This low-coverage ν_{CO}^p behavior therefore points further to the occurrence of edge-site binding on smaller particle "fragments"; these will adsorb CO preferentially due to the high binding energies compared with terrace sites.³⁰ The presence of such "polydispersed" fragments in the C/Pt films also accounts for the long redshifted "tail" seen in the high- θ_{CO} spectra. Similar ν_{CO}^p spectra to those in Figure 3B were also obtained for low-coverage dosing onto the smaller C/Pt nanoparticles, indicating that preferential CO binding again occurs at edge sites. The θ_{CO} -dependent form of the spectra in Figure 3B are comparable to those reported for similarly sized SiO_2 -

supported Pt particles in contact with gaseous CO: the latter were also interpreted in terms of edge/terrace site binding.²⁹

Two other pieces of evidence point to the importance of edge-site coordination in the present nanoparticle films. The first is discerned from the ν_{CO}^P - E dependence at lower coverages, as exemplified by the data for 60 and 20% film loadings at the indicated X_{CO} values, plotted in Figure 4B. In contrast to the linear ν_{CO}^P - E dependencies observed for saturated CO layers (Figure 4A), the low X_{CO} data exhibit *nonmonotonic* ν_{CO}^P - E behavior, the ν_{CO}^P frequencies being almost invariant, or even decreasing slightly for $E < -0.05$ V, while increasing sharply ($d\nu_{CO}^P/dE \sim 60 \text{ cm}^{-1} \text{ V}^{-1}$) toward higher potentials (Figure 4B). Interestingly, such ν_{CO}^P - E behavior has been reported previously for low-coverage step-site CO binding on single-crystal Pt electrodes, and attributed to the effects of competitive hydrogen coadsorption at lower potentials.³² The second line of evidence is gleaned from the ν_{CO} bandwidths for saturated CO coverages as a function of particle size, as plotted (open circles, right-hand y axis) in Figure 5. The bandwidths ($\Delta\nu_{1/2}$) are seen to undergo a marked increase in the size range $4 > d > 2$ nm where the ν_{CO}^P values sharply decrease. Most likely, this band broadening reflects the important contributions from both terrace and edge-site CO to the band shape for the smaller nanoparticles, whereas only the former is more dominant for the larger particles ($d > 4$ nm). Nevertheless, the polydispersed nature of the present C/Pt films (i.e., having a distribution of particle geometries) is readily apparent from the large (30–40 cm^{-1}) $\Delta\nu_{1/2}$ values in comparison with those (ca. 20 cm^{-1}) for the truly monodispersed $(\text{Pt}_x\text{CO}_y)^n$ clusters in solution.¹³

Also worthy of note in the present context is a detailed NMR data obtained for CO chemisorbed (from methanol dissociation) on the same C-supported Pt nanoparticles as examined here.^{3,4} Interestingly, the smallest nanoparticles, $d = 2.5$ and especially 2.0 nm, exhibit an enhanced local density of states (LDOS), associated especially with $2\pi^*$ interactions, as deduced from the ^{13}C NMR data.³ This LDOS- d dependence, which correlates with the ν_{CO}^P red-shifts noted here, was suggested to arise from interaction between the Pt nanoparticles and the conductive carbon support.^{3,4} However, on the basis of the present evidence, coupled with the enhancements of LDOS at step/edge versus terrace sites deduced from DFT as noted above,³⁰ the NMR findings would appear to arise at least partly from an “intrinsic” particle-size effect associated with changing Pt coordination geometries. We compare elsewhere^{16a} the nature of ν_{CO} spectra on the present C-supported Pt nanoparticles obtained by direct solution CO dosing, as described here, and from methanol dissociation, as employed in an earlier IR study⁴ as well as in the NMR experiments undertaken by the Illinois group.³ The latter condition leads to distinctly different ν_{CO} spectra, especially lower ν_{CO}^P frequencies, which are identified with the sub-saturated CO coverages normally attained by methanol dissociation. However, the ν_{CO}^P - d dependence obtained from methanol dissociation and CO solution dosing are qualitatively similar, the smallest nanoparticles ($d < 4$ nm) showing red-shifted ν_{CO}^P frequencies in both cases.

Concluding Remarks

While largely unexplored hitherto, it is clear that EC-IRAS can provide a powerful means of discerning in-situ structural characteristics of transition-metal nanoparticle films. While the electrode-based infrared strategies employed here parallel somewhat those established for examining supported particle catalysts in the gas phase,^{28,30} the ability to control as well as

vary the surface potential in the former systems provide an important additional means of analysis in two distinct ways. First, the sensitivity of the vibrational frequencies to the electrode potential, while in the present cases being structurally uninformative at saturation CO coverages, provides a valuable supplementary diagnosis of binding site coordination at lower coverages. Experience from related ν_{CO} - E behavior at stepped single-crystal electrodes allows a firm structural conclusion of edge- versus terrace-site coordination to be achieved in this case. Second, as already emphasized, the intercomparison of spectra at fixed surface potentials provides at least an approximate separation to be achieved between interfacial field and “chemical bonding” effects. While these notions are at least implicit in a number of electrochemical surface vibrational studies, especially of monocrystalline electrodes, we believe they have not been enunciated previously for metal nanoparticle systems.

Consequently, while not often recognized, the usual lack of surface-potential control for metal particles in gaseous as well as nonelectrochemical solution-phase environments can obfuscate the spectral interpretation, especially given that ϕ_s can be affected greatly by the presence of adventitious redox-active impurities, even in the gas phase.³⁵ As an example, this complication may beset the interpretation of ν_{CO} spectra obtained for metal colloid and related nanomaterials in solution, especially when comparisons with related spectra for metal–UHV systems are undertaken.³⁶ In general, electrochemical and UHV-based metal interfaces are unique in surface science in that the surface potential (electrode potential or work function) is controlled and/or known. While the surface potential may be measurable for metal particles in gaseous or solution-phase environments, it is seldom evaluated. There is good reason, then, to anticipate that the structural characterization of metallic (and semiconducting) particles in controlled-potential (i.e., electrochemical) environments will turn out to have a distinctly broad importance in nanoscience.

Acknowledgment. We are grateful to Andrzej Wieckowski and YuYe Tong for collaborating in our initial examination of these systems (ref 16), and for helpful discussions. This work is supported by the National Science Foundation and the Petroleum Research Fund.

References and Notes

- (1) For example: McBreen, J.; Mukerjee, S. In *Interfacial Electrochemistry*; Wieckowski, A., Ed.; Marcel Dekker: New York, 1999; p 895.
- (2) For example: (a) Frelink, T.; Visscher, W.; van Veen, J. A. R. *J. Electroanal. Chem.* **1995**, 382, 65. (b) He, C.; Kunz, H. R.; Fenton, J. M. *J. Electrochem. Soc.* **1997**, 144, 970. (c) Mukerjee, S.; McBreen, J. *J. Electroanal. Chem.* **1998**, 448, 163.
- (3) Tong, Y.; Rice, C.; Wieckowski, A.; Oldfield, E. *J. Am. Chem. Soc.* **2000**, 122, 1123.
- (4) Rice, C.; Tong, Y.; Oldfield, E.; Wieckowski, A.; Hahn, F.; Gloaguen, F.; Leger, J.-M.; Lamy, C. *J. Phys. Chem. B* **2000**, 104, 5803.
- (5) Chang, S.-C.; Weaver, M. J. *J. Chem. Phys.* **1990**, 92, 4582. (b) Chang, S.-C.; Weaver, M. J. *Surf. Sci.* **1990**, 238, 142.
- (6) Chang, S.-C.; Weaver, M. J. *J. Phys. Chem.* **1991**, 95, 5391.
- (7) Villegas, I.; Weaver, M. J. *J. Chem. Phys.* **1994**, 101, 1648.
- (8) Tang, C.; Zou, S.; Severson, M. W.; Weaver, M. J. *J. Phys. Chem. B* **1998**, 102, 8796.
- (9) (a) Weaver, M. J.; Zou, S.; Tang, C. *J. Chem. Phys.* **1999**, 111, 368. (b) Weaver, M. J. *Surf. Sci.* **1999**, 437, 215. (c) Weaver, M. J.; Wasileski, S. A. *Langmuir* **2001**, 17, 3039.
- (10) Villegas, I.; Weaver, M. J. *J. Phys. Chem. B* **1997**, 101, 10166.
- (11) Corrigan, D. S.; Leung, L.-W. H.; Weaver, M. J. *Anal. Chem.* **1987**, 59, 2252.
- (12) For an overview, see: Weaver, M. J.; Zou, S. In *Spectroscopy for Surface Science, Advances in Spectroscopy*; Clark, R. J. H.; Hester, R. E., Eds.; Wiley: Chichester, U.K., 1998; Vol. 26, Chapter 5.
- (13) Roth, J. D.; Lewis, G. J.; Safford, L. K.; Jiang, X.; Dahl, L. F.; Weaver, M. J. *J. Am. Chem. Soc.* **1992**, 114, 6159.

- (14) Roth, J. D.; Lewis, G. J.; Jiang, X.; Dahl, L. F.; Weaver, M. J. *J. Phys. Chem.* **1992**, *96*, 7219.
- (15) (a) Bjerke, A. E.; Griffiths, P. R.; Theiss, W. *Anal. Chem.* **1999**, *71*, 1967. (b) Lu, G.-Q.; Sun, S.-G.; Chen, S.-P.; Cai, L.-R. *J. Electroanal. Chem.* **1997**, *421*, 19. (c) Zhu, Y.; Uchida, H.; Watanabe, M. *Langmuir* **1999**, *15*, 8757. (d) Ortiz, R.; Cuesta, A.; Marquez, O. P.; Marquez, J.; Mendez, J. A.; Gutierrez, C. *J. Electroanal. Chem.* **1999**, *465*, 239.
- (16) (a) Park, S.; Tong, Y.; Wieckowski, A.; Weaver, M. J. *Langmuir*, submitted. (b) Park, S.; Tong, Y.; Wieckowski, A.; Weaver, M. J. *Electrochem. Comm.*, in press.
- (17) (a) Wasileski, S. A.; Koper, M. T. M.; Weaver, M. J. *J. Phys. Chem. B* **2001**, *105*, 3518. (b) Koper, M. T. M.; van Santen, R. A.; Wasileski, S. A.; Weaver, M. J. *J. Chem. Phys.* **2000**, *113*, 4392.
- (18) (a) ADF version 2000. 03, Department of Theoretical Chemistry, Vrije Universiteit, Amsterdam, 2000. (b) teVelde, G.; Baerends, E. J. *J. Comput. Phys.* **1992**, *99*, 84. (c) Meijer, E. L.; van Santen, R. A.; Jansen, A. P. J. *J. Phys. Chem.* **1996**, *100*, 9282.
- (19) Zoval, J. V.; Lee, J.; Gorer, S.; Penner, R. M. *J. Phys. Chem. B* **1998**, *102*, 1166.
- (20) (a) We have also referred to PDIR Method I earlier as “single potential alteration infrared spectroscopy” (SPAIRS),¹¹ thereby emphasizing the ability to monitor irreversible as well as reversible potential-induced processes. (b) The PDIR Method II is sometimes dubbed alternatively “subtractively normalized interfacial Fourier transform infrared spectroscopy” (SNIFTIRS). However, given the now near-universal use of FTIR spectrometers, this awkward acronym appears also to be superfluous.
- (21) This CO₂ feature, constituting a reliable spectrophotometric monitor of the CO surface concentration, is another important attribute of the present PDIR approach.^{11,12} It has been utilized extensively to extract CO packing densities at oriented single-crystal and other planar electrodes.²²
- (22) (a) Gomez, R.; Feliu, J. M.; Aldaz, A.; Weaver, M. J. *Surf. Sci.* **1998**, *410*, 48. (b) Weaver, M. J.; Chang, S.-C.; Leung, L.-W. H.; Jiang, X.; Rubel, M.; Szklarczyk, M.; Zurawski, D.; Wieckowski, A. *J. Electroanal. Chem.* **1992**, *327*, 247.
- (23) Osawa, M. *Bull. Chem. Soc. Jpn.* **1997**, *70*, 2861.
- (24) (a) Sato, S.; Kamada, K.; Osawa, M. *Chem. Lett.* **1999**, *15*. (b) Sun, S. G.; Cai, W. B.; Wan, L. J.; Osawa, M. *J. Phys. Chem. B* **1999**, *103*, 2460.
- (25) (a) This ν_{CO}^p value (2046 cm⁻¹) was extracted from the ν_{CO}^p - E plot in Figure 8 of ref 13, referring to (Pt₂₆CO₃₂)ⁿ⁻ in dichloromethane, noting that the ferrocene reference electrode employed there has a potential about 0.2 V positive of the aqueous Ag/AgCl used here. (This plot was obtained from the spectroelectrochemical data for a sequence of Pt cluster oxidation states, $-n$, generated by reversible electroreduction/oxidation steps which occur necessarily at discrete redox potentials.) Note that the ν_{CO}^p - E plot accounts for the “quantized” nature of electron charging (i.e., integral n values) for these small nanoclusters by means of an interpolation procedure, discussed in ref 13. Essentially the same ν_{CO}^p value was also obtained for the structurally related (Pt₂₄CO₃₀)ⁿ⁻ cluster. (b) For further discussion regarding the physical significance of surface potential-induced charging of nanoclusters in solution (and gaseous) environments relative to conventional metal-solution interfaces, see: Weaver, M. J.; Gao, X. *J. Phys. Chem.* **1993**, *97*, 332.
- (26) Kharas, K. C. C.; Dahl, L. F. *Adv. Chem. Phys.* **1988**, *1* (Part 2), 70.
- (27) Greenler, R. G.; Burch, K. D.; Kretzschmar, K.; Klauser, R.; Bradshaw, A. M.; Hayden, B. E. *Surf. Sci.* **1985**, *338*, 152–153.
- (28) Hollins, P. *Surf. Sci. Rep.* **1992**, *16*, 51.
- (29) (a) Brandt, R. K.; Hughes, M. R.; Bourget, L. P.; Truszkowska, K.; Greenler, R. G. *Surf. Sci.* **1993**, *15*, 286. (b) Brandt, R. K.; Sorbello, R. S.; Greenler, R. G.; *Surf. Sci.* **1992**, *271*, 605. (c) Kappers, M. J.; van der Maas, J. H. *Catal. Lett.* **1991**, *10*, 365.
- (30) Hammer, B.; Nielson, O. H.; Norskov, J. K. *Catal. Lett.* **1997**, *46*, 31.
- (31) Several Pt coordination geometries mimicking terrace, edge, and vertex sites were modeled with small (Pt_n ≤ 13) clusters. The (111) terrace adsorption site was a center Pt atom in the 7-atom layer, oriented such that the C–O axis is oriented along the C_{3v} axis normal to the surface plane. For a vertex adsorption site, two-layer 4-atom (1, 3) and three-layer 7-atom (1, 3, 3) C_{3v} (111) Pt clusters were employed. The CO molecule was bound to the Pt atom in the 1-atom layer, again such that the C–O axis coincides with the C_{3v} axis. The edge adsorption site utilized a two-layer C_{2v} 9-atom (3, 6) Pt cluster, composed of two parallel rows of three atoms each (A₁, A₂, A₃, and B₁, B₂, B₃) making a (100) plane of 6 atoms. A third row of three atoms (C₁, C₂, C₃) is set exactly on top of the underlying row (B), such that the angle made by connecting the first atom of each row (A₁, B₁, C₁) is 90° and the whole cluster resembles an “L”. The C–O molecule is bound to the center B₂ atom, oriented such that the angle made by “CO”-B₂-A₂ (and likewise “CO”-B₂-C₂) is 135°. The ν_{CO} frequencies for the terrace, 4-atom vertex, 7-atom vertex, and edge adsorption site clusters calculated by DFT are 1999 cm⁻¹, 1947 cm⁻¹, 1965 cm⁻¹, and 1952 cm⁻¹, respectively. [Note that these and other values calculated with the BP86 functional are found to be systematically 4–5% below the experimental values for uncharged (111) surfaces.^{17b}] The vertex and edge adsorption sites, with smaller Pt atom coordination numbers, therefore yield markedly (35–50 cm⁻¹) red-shifted vibrational frequencies with respect to the conventional terrace adsorption sites, in harmony with the experimental estimates for larger Pt particles and stepped Pt surfaces.
- (32) (a) Kim, C. S.; Tornquist, W. J.; Korzeniewski, C. *J. Phys. Chem.* **1993**, *97*, 6484. (b) Kim, C. S.; Korzeniewski, C.; Tornquist, W. J. *J. Chem. Phys.* **1994**, *100*, 628. (c) Kim, C. S.; Korzeniewski, C. *Anal. Chem.* **1997**, *69*, 2349.
- (33) Benfield, R. E. *J. Chem. Soc., Faraday Trans.* **1992**, *88*, 1107.
- (34) (a) Friedrich, K. A.; Henglein, F.; Stimming, U.; Unkauf, W. *Colloids Surf. A* **1998**, *134*, 193. (b) Friedrich, K. A.; Henglein, F.; Stimming, U.; Unkauf, W. *Electrochim. Acta* **2000**, *45*, 3283.
- (35) Weaver, M. J.; Williams, C. T.; Zou, S.; Chan, H. Y. H.; Takoudis, C. G. *Catal. Lett.* **1998**, *52*, 181.
- (36) For example: de Caro, D.; Bradley, J. S. *New. J. Chem.* **1998**, *1267*.